

REPORT DOCUMENTATION PAGE

*Form Approved
OMB No. 0704-0188*

The public reporting burden for this collection of information is estimated to average 1 hour per response, including the time for reviewing instructions, searching existing data sources, gathering and maintaining the data needed, and completing and reviewing the collection of information. Send comments regarding this burden estimate or any other aspect of this collection of information, including suggestions for reducing the burden, to Department of Defense, Washington Headquarters Services, Directorate for Information Operations and Reports (0704-0188), 1215 Jefferson Davis Highway, Suite 1204, Arlington, VA 22202-4302. Respondents should be aware that notwithstanding any other provision of law, no person shall be subject to any penalty for failing to comply with a collection of information if it does not display a currently valid OMB control number.

PLEASE DO NOT RETURN YOUR FORM TO THE ABOVE ADDRESS.

1. REPORT DATE (DD-MM-YYYY) 12/31/2011	2. REPORT TYPE Final Report	3. DATES COVERED (From - To) 3/1/2008 - 09/31/2011
--	---------------------------------------	--

4. TITLE AND SUBTITLE Beam-Shaped Single Mode Spiral Lasers.	5a. CONTRACT NUMBER FA9550-08-1-0047
	5b. GRANT NUMBER
	5c. PROGRAM ELEMENT NUMBER

6. AUTHOR(S) Federico Capasso	5d. PROJECT NUMBER
	5e. TASK NUMBER
	5f. WORK UNIT NUMBER

7. PERFORMING ORGANIZATION NAME(S) AND ADDRESS(ES) Harvard College, Holyoke Center, Suite 600 1350 Massachusetts Ave. Cambridge, MA 02138	8. PERFORMING ORGANIZATION REPORT NUMBER
--	---

9. SPONSORING/MONITORING AGENCY NAME(S) AND ADDRESS(ES) Air Force Office of Scientific Research 875 North Randolph St. Suite325, Rm 3112 Arlington, VA 22203	10. SPONSOR/MONITOR'S ACRONYM(S) AFOSR
	11. SPONSOR/MONITOR'S REPORT NUMBER(S) AFRL-OSR-VA-TR-2012-0208

12. DISTRIBUTION/AVAILABILITY STATEMENT
Approved for public release; Federal purpose rights.

13. SUPPLEMENTARY NOTES

14. ABSTRACT
Using as a model system Quantum Cascade Lasers the Principal investigator demonstrated the performance limitations of spiral shaped cavities as far as their inability to achieve high directionality; he showed that suitably deformed (Limaçon shaped) resonators can partially circumvent this problem and also achieve higher optical power. He then invented notched elliptical resonators demonstrating for the first time highly unidirectional whispering gallery mode microcavity lasers with divergence as small as 5 deg. These lasers have lower threshold current density and far greater beam quality than ridge lasers, and single mode behavior in a limited range of currents. The PI found that the beam divergence is insensitive to the pumping current and to the notch geometry, demonstrating the robustness of notched elliptical resonators. Simulations have also shown that this device efficiently collimates also TE polarized modes that are typical of diode lasers. Thus this resonator can also be used to design highly unidirectional low threshold near-infrared and visible microcavity diode lasers. The successful realization of these simple-structured microcavity devices through standard photolithographic fabrication makes small volume, highly directional light sources possible in the future.

15. SUBJECT TERMS
Quantum cascade laser, limaçon shaped, microcavity semiconductor lasers, ray optics, wave simulations, QCL resonators, beam divergence

16. SECURITY CLASSIFICATION OF:			17. LIMITATION OF ABSTRACT SAR	18. NUMBER OF PAGES	19a. NAME OF RESPONSIBLE PERSON Federico Capasso
a. REPORT U	b. ABSTRACT U	c. THIS PAGE U			19b. TELEPHONE NUMBER (Include area code) 617 384 7611

**Final Performance Report to AFOSR
on AFOSR contract FA9550-08-1-0047
Beam Shaped Single Mode Spiral Lasers
Reported Period: 3/1/2008 - 9/30/2011**

**PI :Prof. Federico Capasso
School of Engineering and Applied Sciences
Harvard University
205A Pierce Hall, 29 Oxford St.
Cambridge MA 02138
Tel. 617-3847611
Fax 617-495-2875
Email: capasso@seas.harvard.edu**

1. Objectives

The objective of this contract was to design new semiconductor lasers with deformed resonators, in particular spiral shape ones and other shapes as well, with the goal of circumventing the limitations of whispering gallery mode lasers and in particular to achieve single mode emission with controlled beam shaping, such as high directionality.

2. Accomplishments

a. Performance Limits of spirals shaped lasers.

The PI's initial investigations (R. Audet et al. Appl. Phys. Lett. **91**, 131106 (2007)) of mid-infrared spiral quantum cascade laser (QCL) had demonstrated a very interesting feature: the far field showed emission in multiple directions and did not appear to be diffracted out by the notch, as it was initially predicted and observed in short wavelength spiral lasers. Modeling also showed that only by pumping a selected area around the device boundary could lead to directional emission. The impracticality of this solution (increased spreading resistance, etc.) led to research into new resonators with highly directional laser emission based on whispering gallery mode lasers: the limaçon-shaped microcavity laser and the notched- elliptical resonator microcavity laser.

b. Limaçon-Shaped directional microlasers

A limaçon-shaped microcavity had been proposed (J. Wiersig and M. Hentschel, Phys. Rev. Lett. **100**, 033901 (2008)) as a promising resonator shape for microcavity lasers with attractive properties such as a directional emission and a high cavity quality-factor (Q-factor). The PI's team modeled $\lambda \approx 10 \mu\text{m}$ quantum cascade lasers (QCLs) with limaçon-shaped microcavity and then fabricated them and tested their performance. Both ray optics and wave simulations showed that in a significant range

of deformations, these microcavities support high quality-factor whispering gallery-like modes (WGM) while having a directional far-field profile with a beam divergence $\theta_{//}=30^\circ$ in the plane of the cavity. The measured far-field profiles were in good agreement with simulations (C. Yan et al. *Applied Physics Letters* **94**, 251101 (2009)). While the measured spectra showed a transition from whispering gallery-like modes to a more complex mode structure at higher pumping currents, the far field was insensitive to the pumping current demonstrating the predicted “universal far-field behavior” of this class of chaotic resonators, an important result in the physics of chaotic resonators. Due to their relatively high quality factor, these microcavity lasers displayed reduced threshold current densities compared to conventional ridge QCLs with millimeter-long cavities. The performance of the limaçon-shaped QCLs was further shown to be robust with respect to variations of the deformation near its optimum value of $\varepsilon=0.40$.

c. Highly directional whispering gallery mode lasers with elliptical notched resonators

The PI discovered that elliptical resonators with a notch at the boundary support in-plane highly unidirectional laser emission from WGMs with divergence substantially smaller than limaçon-shaped lasers and with complete suppression of side lobes. The notch acts as a scatterer that preserves the Q-factor of the WGMs. Using mid-infrared ($\lambda \sim 10 \mu\text{m}$) injection quantum cascade lasers as a model system, an in-plane beam divergence as small as 6 degrees with a peak optical power of $\sim 5 \text{ mW}$ at room temperature was been demonstrated. The beam divergence is insensitive to the pumping current and to the notch geometry, demonstrating the robustness of this resonator design. The latter is scalable to the visible and the near-infrared, thus opening the door to very low threshold highly directional microcavity diode lasers. Simulations have also shown that the notched elliptical resonator efficiently collimates also TE polarized modes that are typical for diode lasers. Thus this new resonator can also be used to achieve highly unidirectional near-infrared and visible WGM lasers. Furthermore, the successful realization of these simple-structured microcavity devices through standard photolithographic fabrication makes small-volume directional light sources possible for many important applications in, e.g. photonic integrated circuits (PICs), optical communications, and medical/biological high-sensitive sensors

d. Multibeam low divergence lasers with elliptical collimators

The PI's team designed a new class of plasmonic lenses that generate multiple free-space beams in arbitrary directions from a point source of surface waves, using a phenomenological model which accurately predicts their far-field, in amplitude, phase and polarization. The researchers fabricated such plasmonic lenses consisting of elliptically shaped metallic structures on the facets of QCLs. As an example of application, they demonstrated ($\lambda \sim 8 \mu\text{m}$) dual-beam emission from QCLs and showed the versatility of the concept by realizing different emission directions with low

divergence. The plasmonic lenses demonstrated here are generally relevant for interfacing of nano-scale optical components to free-space beams.

3. Performance limits of spiral shaped semiconductor lasers

Microcavity lasers show great promise as low-threshold, single-mode lasers suitable for high density integration. They are also fascinating to study as unique model systems combining problems from both quantum chaos and nonlinear laser physics.

The PI collaborated with the group of Martina Hentschel of the Max Planck Institute for Complex Systems in Dresden (Germany) perform ray and wave simulations of passive and active spiral-shaped optical microcavities, comparing the results to experimental data obtained with mid-infrared quantum cascade spiral microlasers. Spiral microcavity lasers have received particular attention in recent years. The devices possess a “notch” Fig. 1(a), which breaks the symmetry of the resonant cavity and potentially allows for unidirectional laser emission. The PI and his collaborators demonstrated that ray simulations are a useful and versatile tool for predicting the angular emission properties of spiral microcavities. The far-field

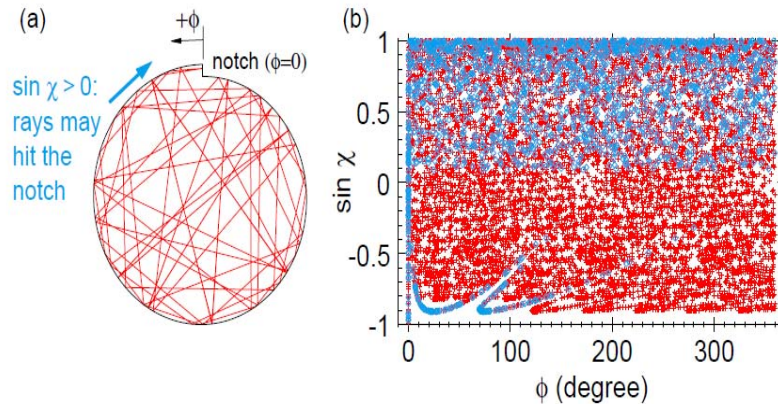


Fig. 1. (a) Spiral microcavity ($\varepsilon = 0.1$) with sample trajectory and (b) phase space portrait (red crosses). The blue diamond symbols mark a snapshot in the Poincaré SOS at the 4th bounce. See text for details.

profiles of spiral microlasers with TM-polarized laser modes (as is the case for QC lasers) were simulated using ray simulations of spiral Fresnel billiards. The advantage of ray simulations over wave calculations is their greater computational efficiency, which allows one to make predictions with extremely low numerical effort. A sample trajectory and the corresponding phase space in the form of a Poincaré surface of section (SOS), taken at the cavity boundary for the spiral resonator shown in Figs. 1(a) and (b), respectively.

The Poincaré SOS was obtained by starting 170 test rays in a clockwise direction

with random initial conditions and then following them over 20 bounces (shown as red crosses). There are no islands of stability visible in Fig. 1(b). In contrast to disk resonators, angular momentum is not conserved in the spiral resonators because of the non-constant (decreasing or increasing, depending on the sense of rotation) radius of curvature. All rays started in the clockwise direction ($\sin\chi > 0$) will eventually hit the notch and thereby change their sense of rotation to counter-clockwise ($\sin\chi < 0$). The blue diamond symbols in Fig. 1(b), which present a snapshot of the test rays taken at the fourth bounce, illustrate how this happens. By the fourth bounce, most of the rays that started in the clockwise direction have not yet hit the notch; hence, coverage of the upper half ($\sin\chi > 0$) of the Poincaré SOS is essentially uniform. Rays that hit the notch on one of the first four bounces have changed their sense of rotation to counterclockwise ($\sin\chi < 0$) and correspond to the blue, nearly connected, “tentacle structures” in the lower half of Fig. 1(b). As the notch is located at $\Phi = 0$, the vertical signature in the Poincaré SOS at this position indicates the route to counter-clockwise rotation: the position angle Φ for all the rays hitting the notch is zero and the angles of incidence χ vary. The tentacle-type signatures that consist of blue diamonds in the lower half of Fig. 1(b) ($\sin\chi$ close to -1) correspond to the next bounces (up to 3) of the rays that hit the notch at $\Phi = 0$ and change their sense of rotation. These trajectories typically hit the boundary under a rather large angle $|\chi|$. The distinct structure in phase space is formed because the small spatial extent of the notch defines a limited set of initial conditions associated with hitting the notch. The tentacle signatures blur over the next few bounces, but can still be recognized as such before the chaotic character of the resonator dominates the long-time dynamics. Focusing on the angular emission characteristics, the PI found that both ray and wave simulations are consistent with the experimental data, showing richly-featured, multidirectional far-field emission patterns in the case of uniform pumping and TM-polarized light. Active cavity simulations using the Schroedinger-Bloch model indicate that *selective* pumping of the quantum cascade spiral microlasers near the resonator boundary will yield unidirectional laser emission (Fig. 2).

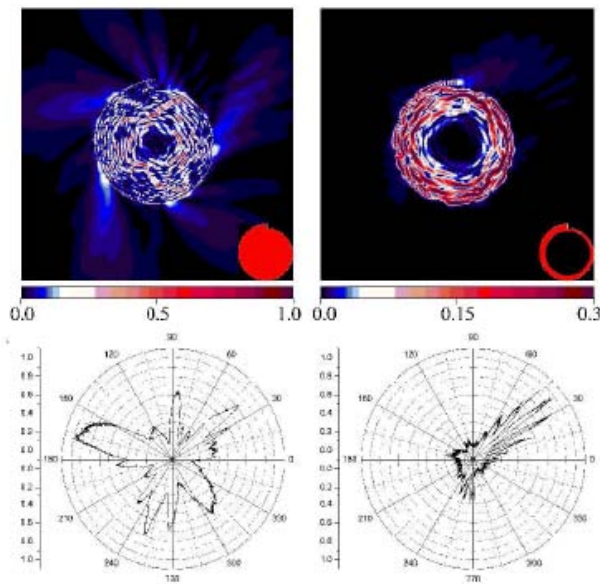


Fig.2 Uniform (left panels) and boundary (right panels) pumping of spiral-shaped microlasers. The area pumped is shown in the insets; in the case of selective pumping the boundary area pumped is at least $0.1r_0$, where r_0 is the minimum radius of the spiral. The upper panels show snapshots of the intensity distribution in the lasing cavity. The lower panels show the far-field patterns for pumping strength slightly above the lasing threshold as a function of angle. The uniformly pumped device (left) has multidirectional laser emission, whereas the boundary-pumped device (right) has pronounced directional emission

4. Limaçon-Shaped directional microlasers

a. Simulations

The boundary of a Limaçon microcavity is defined in polar coordinate as $R(\theta) = R_0(1 + \varepsilon \cos \theta)$ where ε is the deformation factor and R_0 is the radius of curvature when $\theta = \pi/2$ (see the inset of Fig. 3(a)). In this work, the PI team first carried out wave simulations based on the boundary element method to study the effect of the parameter ε on the key characteristics of the limaçon microcavity QCLs such as Q-factor and directionality of the light emission. Note that the polarization of QCL is transverse magnetic (TM) due the selection rules of the optical transition. The effective refractive index of our QCL material (lattice matched $\text{Ga}_{0.47}\text{In}_{0.53}\text{As}/\text{Al}_{0.48}\text{In}_{0.52}\text{As}/\text{InP}$) for TM polarization, n , is estimated to be 3.2, calculated from spectral measurement of the mode spacing of a Fabry-Perot type ridge laser. Figs. 3 (a-c) show the intensity distribution of some TM modes calculated for a structure with $\varepsilon = 0.40$ and $R_0 = 80 \mu\text{m}$. The two highest Q-factor modes are shown, respectively, in Figs. 3 (a) and (b); they both have a calculated Q-factor $> 10^7$.

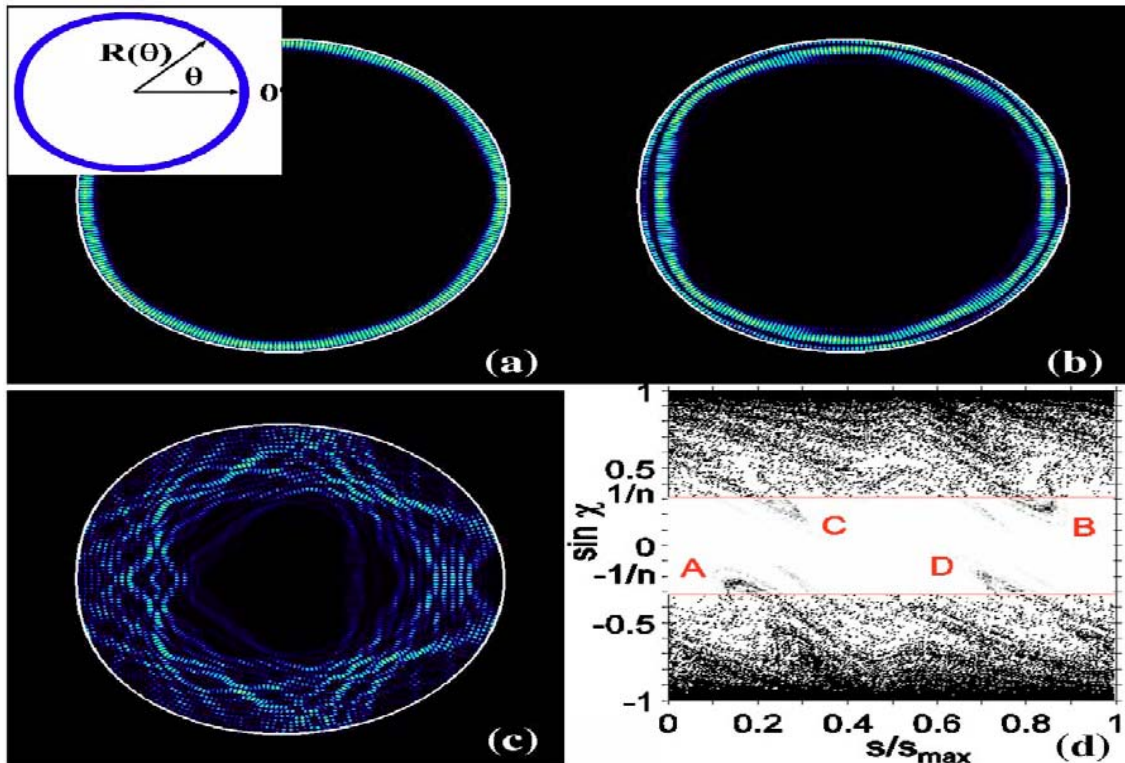


Fig. 3 (a-c) Intensity distribution of the TM modes inside the cavity calculated with wave simulations ($\varepsilon=0.40$ and $R_0=80 \mu\text{m}$); (d) Poincaré Surface of Section (SOS) of rays leaving the limaçon cavity where s (measured from the $\theta = 0$ direction with s max being the cavity circumference) is the arc length and χ is the angle of incidence at each reflection at the cavity boundary.

Since these whispering gallery-like modes have the highest Q-factor, they can be excited at pumping currents just above the lasing threshold. The mode in Fig. 3 (c) is a non-WGM which has a lower Q-factor of about 18,000 and as such it is expected that this type of mode will be excited at higher pumping currents. Fig. 3 (d) shows the Poincaré surface of section (SOS) of rays leaving the Limaçon cavity with $\varepsilon = 0.4$ and $R_0 = 80 \mu\text{m}$ calculated with ray optics simulations. The character of the ray trajectories is chaotic, while the far-field profile is determined by the path in phase space that the rays take to escape the cavity by entering the leaky region, where the condition of total internal reflection is not fulfilled anymore.

Both wave and ray optics simulations show that the deformation $\varepsilon = 0.40$ results in the smallest far-field divergence angle (defined as the full-width at half-maximum (FWHM) of the main far-field lobe around $\theta = 0$ line). The divergence angle of the optimal structure is about 30° as shown in Fig. 4(a) by the solid line (ray optics simulation) and the dash dotted line (wave simulation), which are in overall good agreement. The inset of Fig. 4 (a) shows the external intensity distribution of the mode in Fig. 3 (a) obtained by wave simulation. The main peaks are labeled as A', B', C' and D' corresponding to the escape regions A, B, C, D, respectively, as marked in Fig. 3 (d). Interestingly, it was observed (Fig. 4 (b)) that all three modes in Figs. 3 (a-c) show similar external far-field profiles no matter whether they are high Q-factor whispering gallery-like modes or low Q-factor non-WGMs. This is what is called "universal far-field behavior", which was also observed previously in quadrupole deformed microcavities (S. B Lee et al. Phys. Rev. A **75**, 011802(R) (2007)). The reason for this "universal far-field behavior" is that the emission directionality is mainly determined by the structure of the unstable manifolds in the leaky region, as shown in Fig. 3 (d), which are determined by the geometric shape of the deformed microcavity, regardless of the different spatial distributions of these modes.

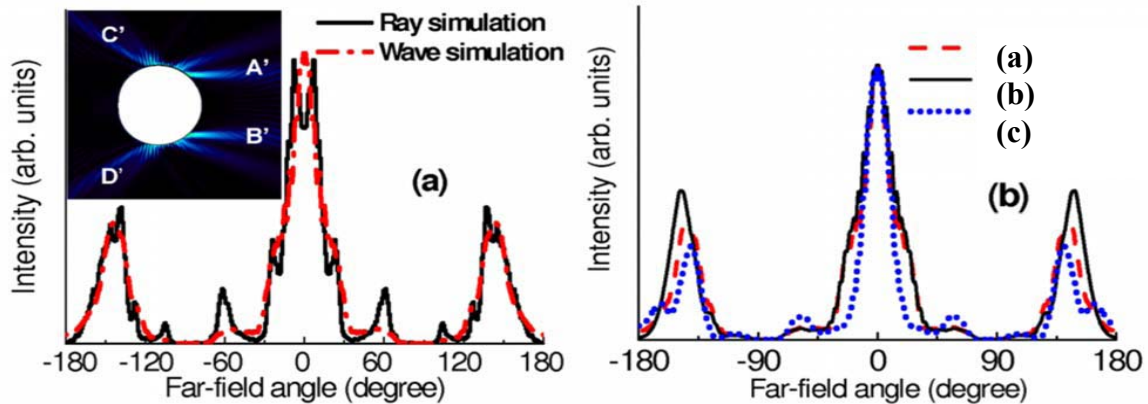


Fig. 4 (a) Comparison of the far-field profiles obtained with wave simulation corresponding to the optical mode in Fig. 3(a) and ray optics simulation; the inset is the external intensity distribution of the mode in Fig. 3(a); (b) Wave simulations of the far-field profiles of the three modes in Figs. 3. All profiles are normalized to their maximum values.

b. Fabrication and Testing

The QCL material used was similar to the one described in a recent paper (N. Yu et al. *Nature Photonics* **2**, 564 (2008)) but with a different doping level ($\sim 30\%$ lower) in the active region. Devices with different sizes $R_0 = 50, 80,$ and $110 \mu\text{m}$ and deformations ε ranging from 0.20 to 0.80 were fabricated. Inductively coupled plasma reactive ion etching (RIE) was used to etch the QCL material to obtain microcavities with smooth sidewalls. The top view and the side view of a typical device are shown in the inset of Fig. 5. The sidewall roughness is about 300 nm, which is expected to result only in minor scattering of the mid-infrared radiation.

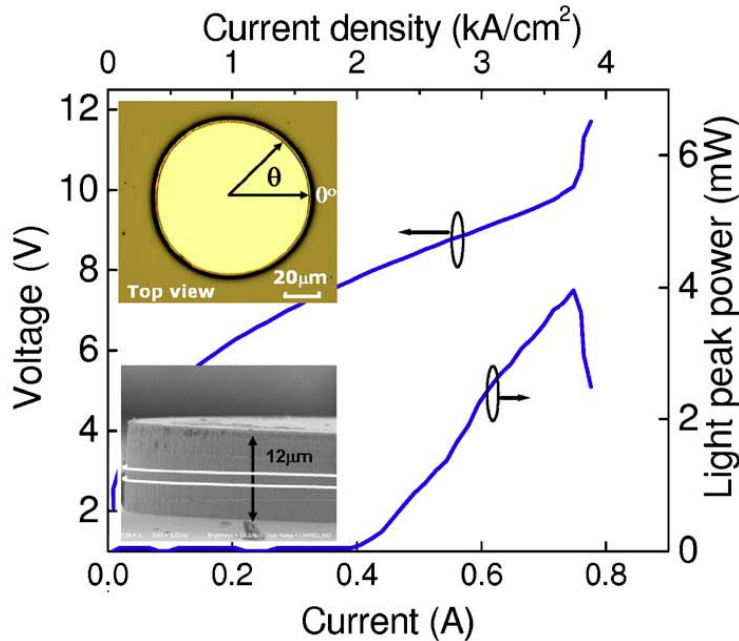


Fig. 5 Voltage and peak output power as a function of injection current for the Limaçon-shaped microcavity quantum cascade laser with a deformation factor $\varepsilon = 0.40$ and $R_0 = 80 \mu\text{m}$; the upper left inset is the top view of the device taken with an optical microscope; and the lower left inset is the scanning electron microscope image of the side view of the device; the two white lines indicate the position of the active region.

The processed devices were tested in pulsed mode at room temperature with 125 ns current pulses at 80 kHz repetition rate. All devices demonstrated laser action. Fig. 3 shows the light output power versus current (L-I) and voltage versus current (V-I) characteristics of a representative device with $\varepsilon = 0.40$ and $R_0 = 80 \mu\text{m}$. Peak output power of 4 mW, a maximum slope efficiency of about 12 mW/A, and a threshold current density around 2.0 kA/cm^2 were obtained. This device has a smaller threshold current

density compared with that ($\sim 2.6 \text{ kA/cm}^2$) of ridge QCLs with a length of 2.5 mm and 14 μm width processed from the same wafer.

For this device, a Q-factor of approximately 1200 was obtained based on the measurements of the threshold current density and the gain coefficient (C. Gmachl et al IEEE J. Quantum Electron. **33**, 1567 (1997)). Although the measured Q-factor is smaller than those of shorter wavelength semiconductor lasers (J. Faist et al Appl. Phys. Lett. **69**, 2456 (1996)), as a result of the increase in waveguide losses, it is larger than the Q-factors reported for other circular-shaped QCLs emitting at similar wavelengths. This is assigned to material and device processing improvements and to the limaçon resonator, which supports high Q-factor whispering gallery-like modes. Note that, due to the high optical losses associated with free carrier absorption at mid-infrared wavelength, the measured Q-factor in our devices is much smaller than the value obtained in simulations.

c. Spectral and far field measurements

Figure 6(a) shows the emission spectra of the Limaçon microcavity QCL measured along the $\theta = 0$ direction at different pumping currents with a high-resolution Fourier transform infrared spectrometer (FTIR). The laser operates in single mode at $\lambda \approx 10 \mu\text{m}$ at the threshold current of 380 mA. At a pumping current of 500 mA, two sets of optical modes appeared, indicated by red and blue arrows, corresponding to the two high Q-factor whispering gallery-like modes shown in Figs. 3 (a) and (b), respectively. The average mode spacing of each set is approximately 6.0 cm^{-1} , which agrees very well with the calculated value (6.2 cm^{-1}) for WGMs, given by $1/(L*n)$, where L is the perimeter of the structure. At higher pumping current several additional unequally spaced modes appeared, indicated by green arrows, corresponding to lower Q-factor modes (non-WGMs) of the type shown in Fig. 3 (c). Essentially the same spectra from all far-field lobes in different directions were observed.

The far-field profiles of the devices were measured in steps of 0.5° using a setup previously described (N. Yu et al. Nature Photonics **2**, 564 (2008)). The experimental results for a device with an optimal (in terms of the far-field divergence angle) deformation $\varepsilon = 0.40$ are shown in Fig. 6 (b) for pumping currents of 500 mA and 710 mA, together with the ray optics simulation. Excellent agreement is achieved between experiment and simulation. Note that although non-WGMs appear at higher pumping current of 710 mA (see Fig. 6 (a)), the far-field profile is essentially the same as the one pumped at 500 mA showing directional emission due to the "universal far-field behavior" predicted for this type of resonator. The FWHM of the main lobe of the far-field profile is $\sim 33^\circ$, which is close to the theoretically predicted value of 30° . The small discrepancy is most likely due to the surface roughness that broadens the main lobe.

Very good agreement between the calculated and the measured far-field profiles was also observed with ε different from 0.4. Note however, that for ε larger than 0.5, the geometry of the microcavity is such that whispering gallery-like modes are not supported anymore in the cavity; a detail discussion will be reported elsewhere. To further investigate the dependence of the device performance on the deformation factor, the PI team measured

several samples with $\varepsilon = 0.37$ and 0.43 . This range of cavity deformation results in about $5 \mu\text{m}$ difference in the cavity sizes along the short axis for $R_0 = 80 \mu\text{m}$ devices, well within the fabrication resolution of photolithography. The experimental results show that the shape, position, and FWHM of the main lobe of the far-field profiles, as well as the light output power and threshold current densities, are insensitive to the deformation in the range $0.37 < \varepsilon < 0.43$.

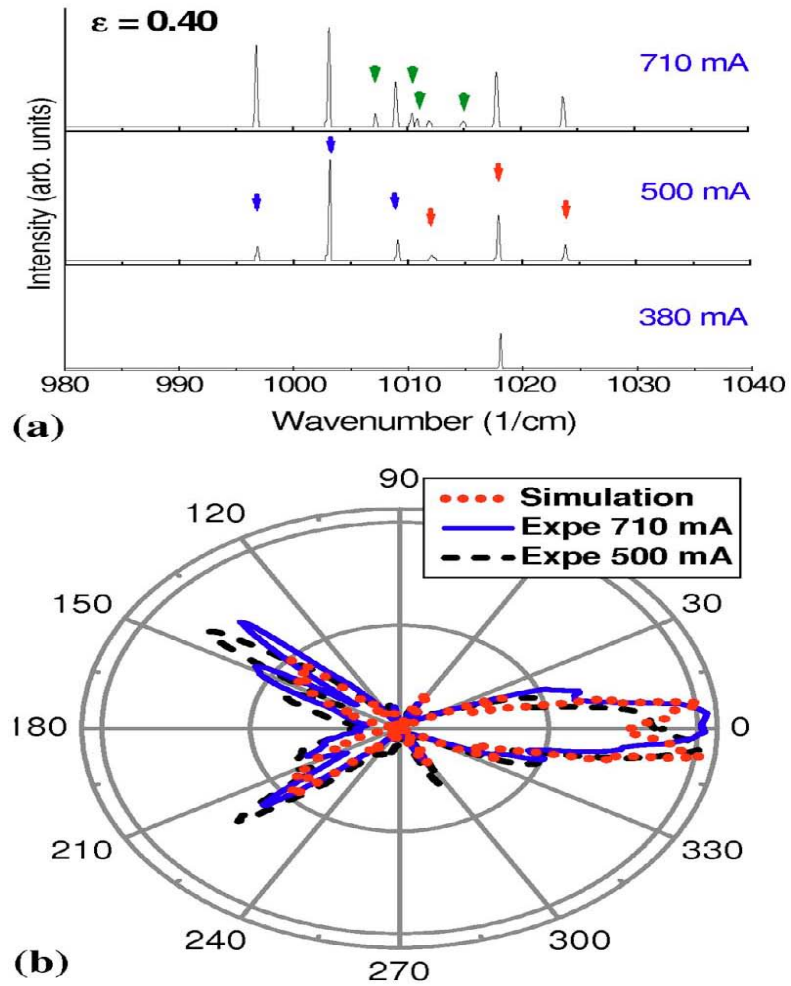


Fig. 6 Experimental results for a limaçon microcavity QCL with $\varepsilon = 0.40$ and $R_0 = 80 \mu\text{m}$. (a) Laser spectra at different pumping currents. The threshold current of the laser is around 380 mA ; at 500 mA pumping current, two sets of WGMs are shown, expected to correspond to the two set modes in Figs. 3(a) and 3(b); at a higher pumping current (710 mA), several non-WGMs appear; (b) Comparison between ray optics simulation and experimental lateral far-field profiles in polar coordinates at pumping currents of 500 and 710 mA . All far-field profiles are normalized to their maximum values.

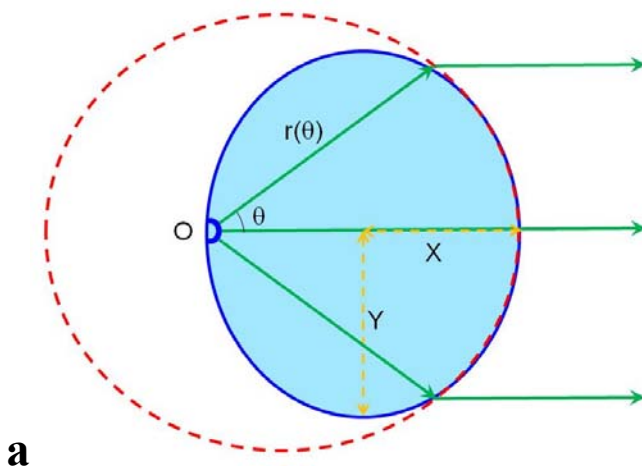
In conclusion, the PI demonstrated theoretically and experimentally low divergence high Q-factor whispering gallery-like modes semiconductor lasers with a Limaçon-shaped microcavity. The universal far-field behavior of this class of chaotic resonators was investigated.

5. Highly directional whispering gallery mode lasers with elliptical notched resonators

The PI team has discovered that elliptical resonators with a notch at the boundary support in-plane highly unidirectional laser emission from WGMs with divergence substantially smaller than limaçon-shaped QCLs and with complete suppression of side lobes. The notch acts as a scatterer that preserves the Q-factor of the WGMs. Using mid-infrared ($\lambda \sim 10\mu\text{m}$) injection QCLs as a model system, an in-plane beam divergence as small as 6 degrees with a peak optical power of ~ 5 mW at room temperature has been demonstrated. The beam divergence is insensitive to the pumping current and to the notch geometry, demonstrating the robustness of this resonator design. The latter is scalable to the visible and the near-infrared, thus opening the door to very low threshold highly directional microcavity diode lasers.

a. Design concept and ray simulations

An elliptical resonator was chosen since it possesses WGMs with very high Q-factors¹ for shapes with various long-to-short aspect ratio Y/X . A notch of size comparable to the wavelength in the material, suitably defined on the boundary will diffract light towards the opposite boundary. Figure 7a illustrates how the aspect ratio Y/X of the elliptical resonator (blue curve) was optimized to achieve maximum collimation. The notch is located at the intersection of the short axis and the boundary (point O). In order to achieve collimation of the majority of the light scattered by the notch, the device design exploits a well-known property of the ellipse: for any given refractive index $n > 1$, one can find an ellipse (auxiliary ellipse) such that all incoming parallel rays are collected into one of its foci, meaning that all rays *starting* from one of the foci are collimated. Note that the notch is located at one of the foci of the auxiliary ellipse (red curve), but not at the focus of the elliptical resonator. The Y/X ratio of the elliptical resonator is now chosen such that its boundary best (*i.e.*, over the largest possible angle 2θ) approximates that of the auxiliary ellipse.



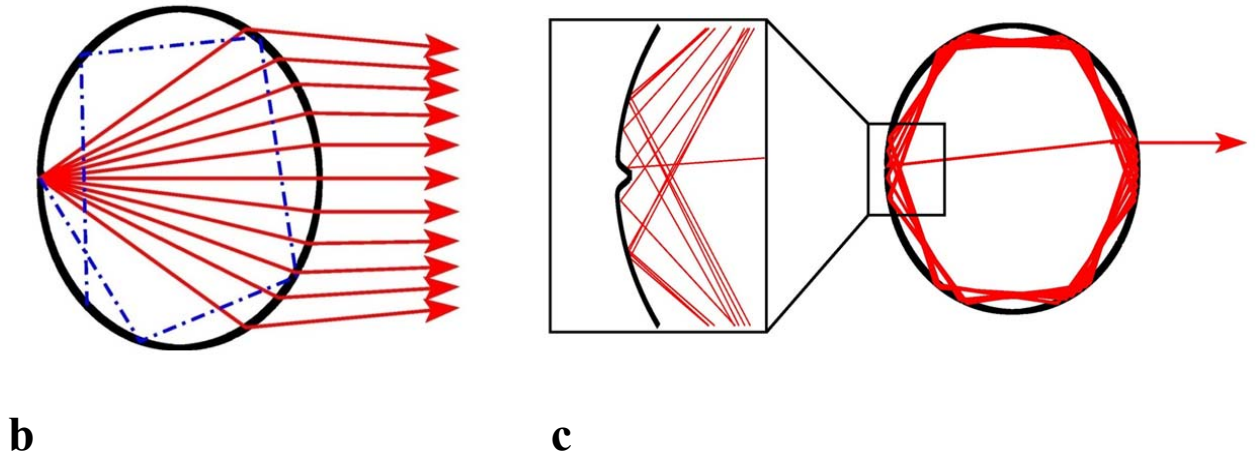
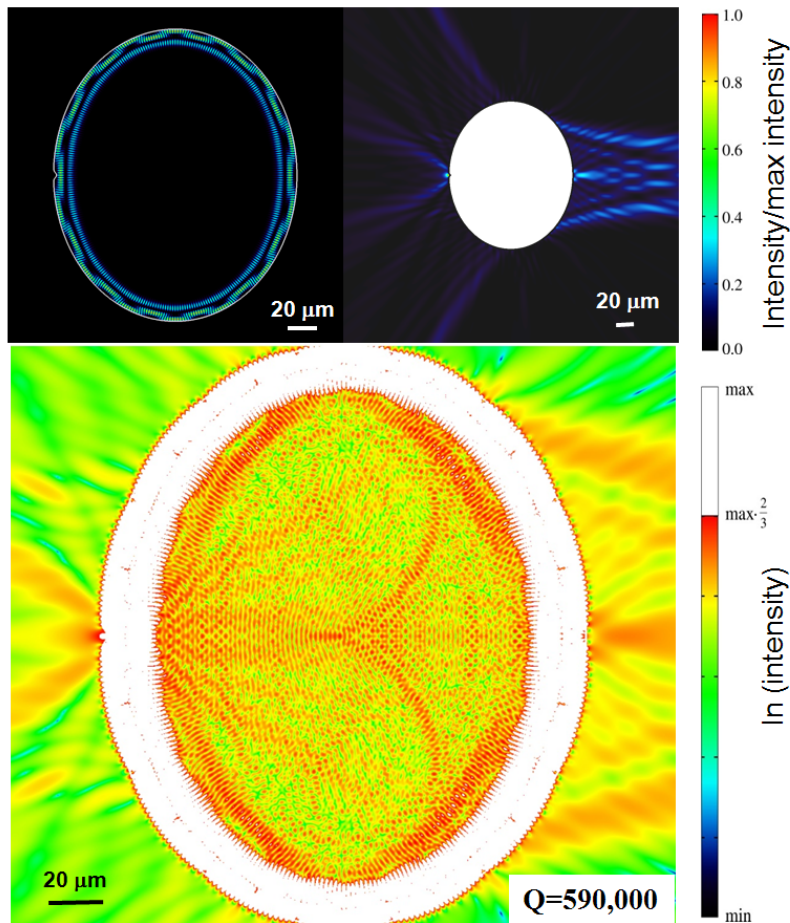


Fig. 7 | Design principle of notched elliptical resonator and simulated ray dynamics. **a**, Schematic illustration of the notched elliptical resonator. The green arrows indicate that light waves are scattered by the notch at point O , then collimated as a parallel beam in the far-field by the right-hand-side boundary of the notched ellipse. The PI utilized the well-known focusing property of the ellipse (auxiliary ellipse in red) to achieve optimal collimation: the boundary of the notched elliptical resonator (blue curve) is designed to best approximate that of the auxiliary ellipse within the largest possible range of $2\theta_{\max}$ (~ 70 deg). The notch of the resonator is located at one of the foci of the auxiliary ellipse (red curve). The optimal Y/X ratio is 1.2 for $n_{\text{eff}} = 3.2$. **b**, Ray simulation of the collimation effect: a number of rays are started at the position of the notch with different outgoing angles, simulating a scattering process. They travel inside the cavity until they hit its boundary, upon which they either are specularly reflected or, if the angle of incidence at the surface is smaller than the critical angle for total internal reflection, get refracted out. The red, solid rays, which leave the notch under relatively smaller outgoing angles, get collimated; the collimation is worse for higher outgoing angles (outermost red rays). The blue dash-dotted ray leaves the notch at a high outgoing angle and is re-launched into a whispering gallery mode. **c**, Ray simulation of whispering gallery mode dynamics. A single ray is started at some position along the resonator boundary with an initial condition such that the angle of incidence is larger than the critical angle. It is then specularly reflected many times, corresponding to a whispering gallery like mode, until at some point it hits the notch. It then gets reflected to the opposite boundary, is refracted out and leaves the cavity parallel to the x -axis due to the collimation effect. A magnification of the dynamics near the notch is shown.

b. Wave simulations

The PI calculated the optical modes in the cavity through wave simulations. Fig. 8 (top) shows the intensity distribution of the first-radial-order WGM which is a transverse magnetic (TM) mode, as QCLs are TM polarized due to the intersubband transition selection rule, for a structure with $Y/X = 1.2$ and an optimized, in terms of minimum beam divergence, notch size $o = 3 \mu\text{m}$ and $d = 2 \mu\text{m}$, where o and d refer to the width and the depth of the notch, respectively; see Fig. 9. A Q-factor as high as 590,000 is calculated for this mode without considering the material optical losses, which are dominated at the mid-infrared wavelengths of QCLs by free carrier absorption. Inclusion of such losses in the simulation, as discussed later in the paper, leads to a much reduced

Q-factor. Fig 8 (top) shows the near-field intensity distribution outside the cavity (right) and the intensity distribution in a logarithmic scale inside the cavity (left), respectively. Only the outermost part of this mode has an overlap with the notch, thus giving a high Q-factor. Light is scattered by the notch to the right-hand-side boundary of the resonator (Fig. 7 (b)). The refracted beams propagate almost parallel to the $\theta = 0$ direction, resulting in unidirectional emission, see Fig. 7 (c). Higher-radial-order, lower Q-factor, WG-like modes are also present. Although the proposed scheme is demonstrated in a regime where the ratio of cavity size to wavelength in material $X/\lambda_{\text{eff}} \sim 26$ is relatively high, simulations show that the smallest notched elliptical resonators with directional emission correspond to $X/\lambda_{\text{eff}} \sim 3$. Simulations demonstrate that the far-field profile of transverse electric (TE) polarized modes is also highly directional, implying that the proposed concept is broadly applicable also to diode lasers operating in the near infrared and visible. High Q whispering gallery modes are preserved in these structures for the same wavelength-to-size ratio. At relatively short wavelengths, e.g. $\lambda \sim 1\mu\text{m}$, free carrier absorption is negligible and optical losses are small ($\sim 0.5\text{ cm}^{-1}$), limited by sidewall roughness of the cavity, and material absorption. This will lead to a much smaller Q-factor degradation than that at mid-IR wavelengths (optical loss is $\sim 15.6\text{ cm}^{-1}$ for our QCLs). Thus notched-elliptical resonators are expected to be excellent also for low-threshold, highly directional microcavity diode lasers.



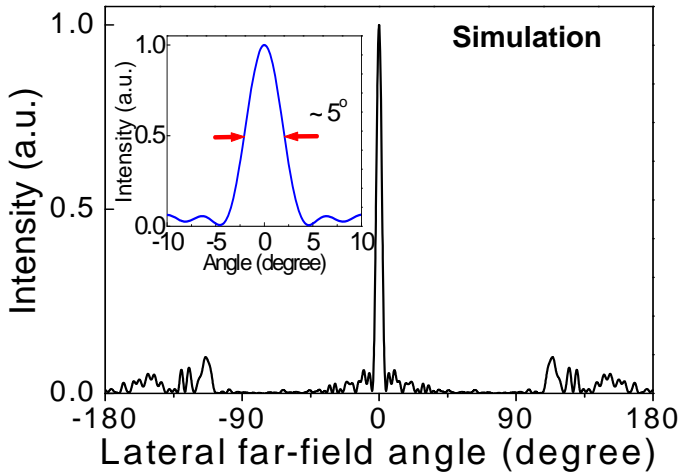


Fig. 8 | Mode distribution by wave simulations. Top left: Calculated mode intensity distribution of a device with $X = 80 \mu\text{m}$ and $Y = 96 \mu\text{m}$ and an optimized notch $o = 3 \mu\text{m}$ and $d = 2 \mu\text{m}$ in linear scale. The free space wavelength is $\lambda = 10 \mu\text{m}$; and $\lambda_{\text{eff}} \sim 3.1 \mu\text{m}$ is the wavelength in material. Shown is the first-radial-order WGM with even parity with respect to the short axis of the resonator. Top right: External near-field intensity distribution of the mode shown on the left. The majority of the output power is collimated along the $\theta = 0$ direction. Middle panel: The same mode intensity distribution of the mode is plotted in a logarithmic scale. Bottom panel: Simulated far-field intensity distribution showing an in-plane beam divergence angle as narrow as $\sim 5^\circ$. The inset shows the zoom-in plot of the far-field intensity profile.

c. Fabrication and Testing

Devices with different dimensions and notch sizes were fabricated and tested in pulsed mode operation at room temperature. Fig. 9 shows scanning electron microscope (SEM) images of a representative device and its vertical sidewall. Also shown is the light output power versus current (L-I) characteristics of this device. The measured Q-factor of our devices is ~ 1260 , deduced from threshold current density and the gain coefficient measurements, which agrees well with the simulation value when the relatively high optical losses at the mid-infrared wavelengths ($\sim 15.6 \text{ cm}^{-1}$ for our devices, deduced from the measurements of threshold current densities versus cavity lengths of ridge laser devices) are included in the simulation. Thus for the QCL case, the threshold current density and Q-factor of the notched elliptical lasers are similar to those of Limaçon-shaped QCLs, respectively, due to the high optical losses.

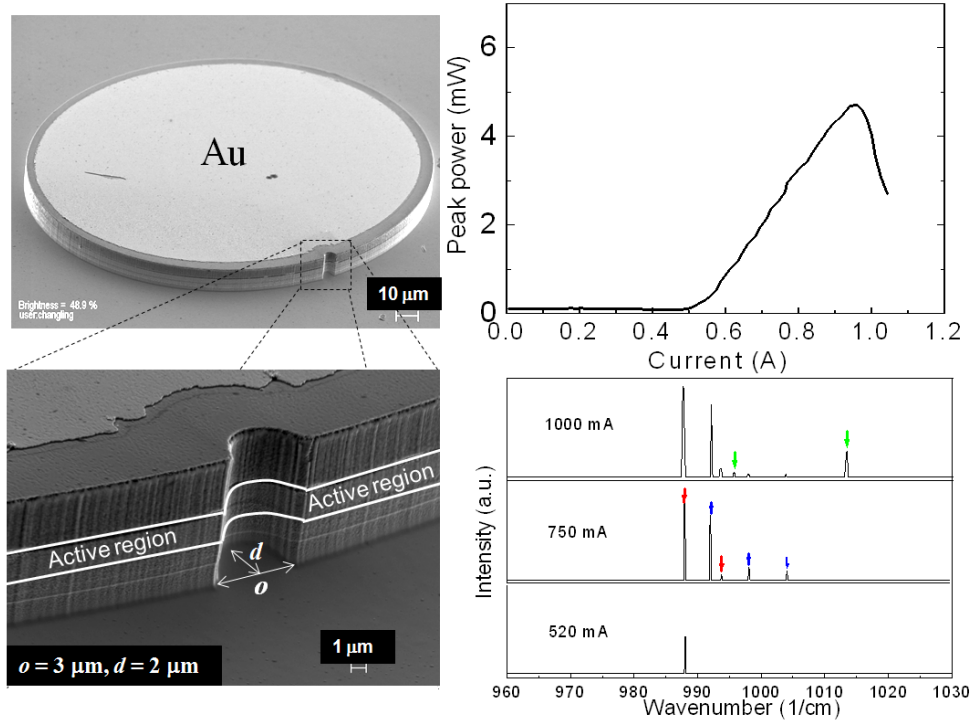
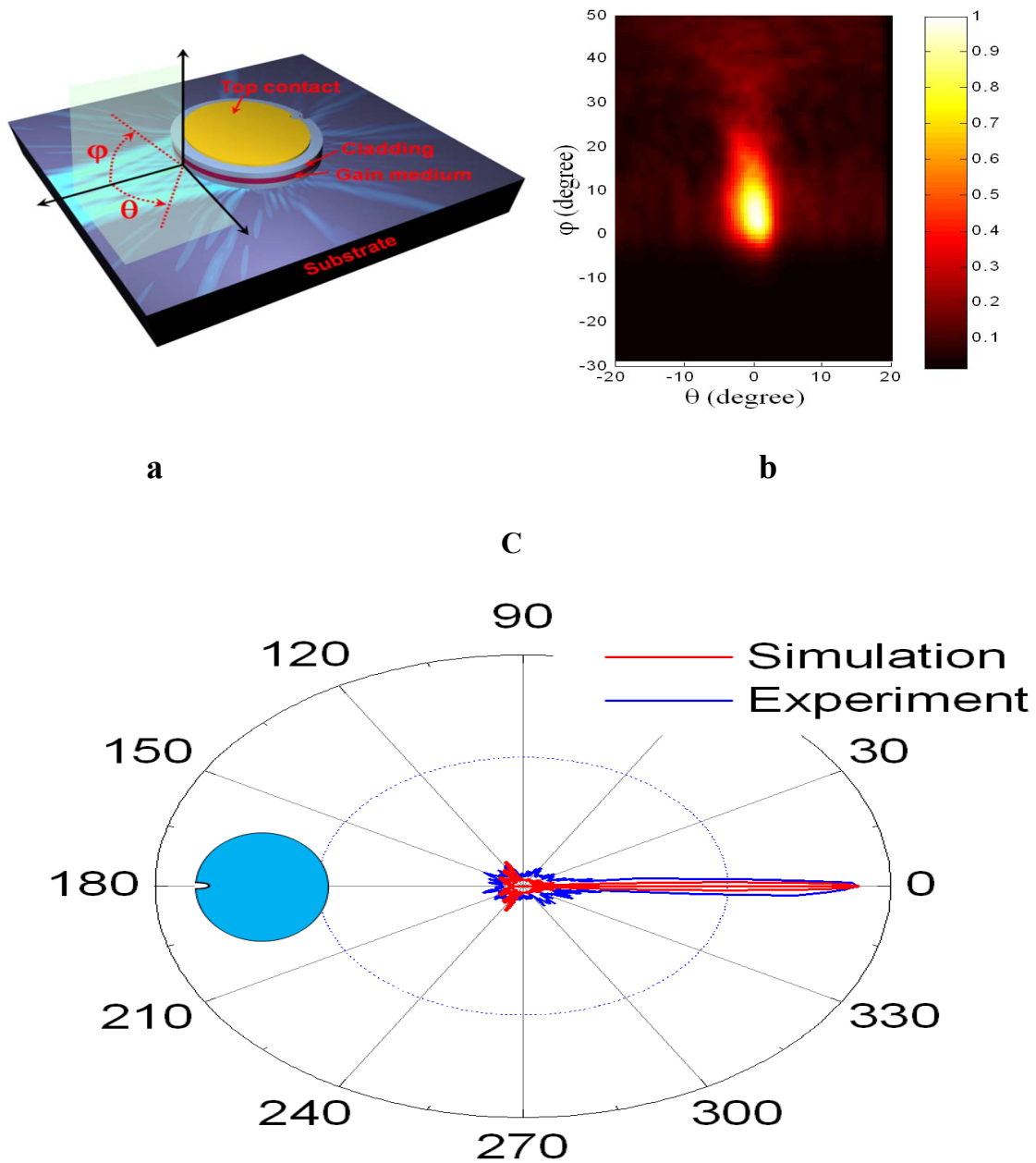


Fig. 9 | Fabricated device and its electrical and optical characteristics. Top left: Scanning electron microscope image of the notched elliptical resonator with a minor radius $X = 80 \mu\text{m}$, a major radius $Y = 96 \mu\text{m}$ and notch dimensions $o = 3 \mu\text{m}$, and $d = 2 \mu\text{m}$. The top gold contact is deposited for electric pumping. Bottom left: zoom-in view of the device showing the smooth sidewall of the laser cavity. The two white lines indicate the boundaries of the active region. c, Room temperature light-current (L-I) characteristics of the device measured in pulsed mode operation with a duty cycle of 1%. A peak output power of $\sim 5 \text{ mW}$, a threshold current density $\sim 2.0 \text{ kA/cm}^2$, and a slope efficiency of $\sim 11 \text{ mW/A}$ were obtained. Bottom right: the laser spectra of the device at different pumping currents. The threshold current of the laser is around 520 mA. At a pumping current of 750 mA, two sets of WGMs, indicated by the blue and red arrows, are present; at an even higher pumping current (1000 mA), several additional modes appear, indicated by green arrows, corresponding to lower Q-factor modes.

d. Spectral and far-field measurements

Fig. 9 presents also the emission spectra of the notched elliptical QCLs measured at different pumping currents. The laser operates in single mode at $\lambda \sim 10 \mu\text{m}$ near the threshold current (520 mA), corresponding to the mode with the highest Q-factor ($> 5 \times 10^6$) with odd parity. At a pumping current of 750 mA, two sets of optical modes appear, indicated by blue and red arrows, corresponding respectively to the first two highest Q-factor WGMs with even and odd parities. The average mode spacing of each set is approximately 5.80 cm^{-1} , which agrees very well with the calculated value of 5.85 cm^{-1} for both odd parity and even parity modes. At a higher pumping current several additional modes appear, indicated by green arrows, corresponding to lower Q-factor type of modes.

The schematic and the two-dimensional far-field of the device are displayed in Figs. 10a and b, respectively. A much narrower beam divergence angle of 6 deg in the plane of the laser cavity than previously reported in microcavity and Fabry-Perot ridge QC lasers is demonstrated. Good agreement is observed between the experimental and simulated far-field intensity profiles (Fig. 10c). The measured vertical far-field divergence angle is about 25 deg. All the far-field profiles are essentially the same at different pumping currents from 720 mA to 920 mA (Fig. 10d). The far-field profiles (Fig. 10e) are insensitive to variations of the notch sizes from 2 μm to 4 μm , a deviation well within fabrication uncertainties.



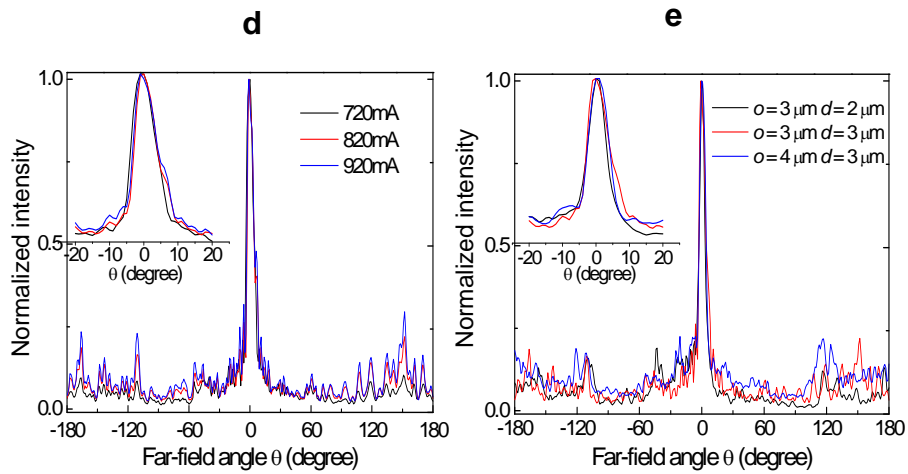


Fig. 10 | Far-field profiles of different microcavity lasers. *a*, Schematic of the device. *b*, Measured two-dimensional far-field intensity distributions of a representative device with a minor radius $X = 80 \mu\text{m}$, a major radius $Y = 96 \mu\text{m}$ and a notch dimension $o = 3 \mu\text{m}$, $d = 2 \mu\text{m}$ at a pumping current of $\sim 720 \text{ mA}$. *c*, The experimental (blue line) and simulated (red line) in-plane far-field intensity profiles in polar coordinate for the device in *b*. The measurements were taken at a current of 720 mA . The small discrepancy between the wave simulation and the measured data is most likely due to the surface roughness that broadens the main lobe of the emission. The far-field profiles are normalized to their maximum values. The simulated far-field profiles of two high Q-factor modes with even and odd parities were included since at the above pumping current both modes exist in the cavity. As the power out-coupling of the even parity mode is much higher than that of the odd parity mode, the overall far-field intensity profile is dominated by the mode with even parity. *d*, Measured far-field profiles of the device in *b* at different pumping currents of 720 mA , 820 mA , and 920 mA , respectively. The inset is the zoom-in plot of the far-field profiles from -20 deg to $+20 \text{ deg}$. *e*, Comparison of the measured far-field profiles for devices with slightly different notch sizes near the optimum $o = 3 \mu\text{m}$, $d = 2 \mu\text{m}$. The insets are the zoom-in plots of the far-field profiles.

6. Multibeam low divergence lasers with elliptical collimators

The PI's group designed a new class of plasmonic lenses that generate multiple free-space beams in arbitrary directions from a point source of surface waves, using a phenomenological model which accurately predicts their far-field, in amplitude, phase and polarization. The PI's team fabricated such plasmonic lenses on the facets of semiconductor lasers. The plasmonic lenses proposed here are generally relevant for interfacing of nano-scale optical components to free-space beams.

In the last few years the PI showed that a one dimensional plasmonic structure integrated on the facet of a QCL leads to a major reduction of the divergence in the vertical direction. In subsequent work he showed that ring shaped 2D structures could achieve a fully collimated beam .i.e. with reduced divergence in perpendicular directions. For a recent

reviews of the above developments see N. Yu and F. Capasso *Journal of Optical Society of America B* **27**, 18 (2010) and N. Yu et al. *IEEE Transactions on Nanotechnology* **9**, 11 (2010).

a. Theory

Designing more complex 2D structures using standard simulation tools, such as finite-difference time-domain (FDTD) or finite-element methods (FEM), is made very difficult by the large size of the 3D simulations required, typically on the order of 10^7 to 10^8 mesh cells.

The essential physical phenomenon involved in a plasmonic collimator is the interference between the emissions of scatterers distributed along the surface, whether they are holes, particles, grooves or ridges. A phenomenological model was introduced by Capasso's team to calculate the far-field radiation pattern of any 2D grating, which approximates the field scattered by the grating as that of an ensemble of electric dipoles distributed on the surface. The simulation time is reduced to several minutes on a personal computer.

While ray tracing models have already been used to describe two-dimensional focusing holographic gratings our dipolar model is more versatile. In particular, by using a 'microscopic' description of the grating, it enables accurate modeling of complex structures with finite size and local parameters that can be varied at will (illumination intensity, scattering efficiency, losses, etc...). The PI used this model to devise a general class of plasmonic lenses that collimate light originating from a single point source and direct it into one or several free-space beams propagating along arbitrary off-axis directions, thus enabling flexible interfacing of plasmonic devices with complex optical systems.

Let us consider a point source O that launches surface waves (SWs) along a corrugated metal-air interface, and an ensemble of point scatterers S lying on the lines C_m in the x-y plane (Fig. 11(a)). A point source approximates well a source of sub-wavelength dimensions such as an aperture milled in the metallic film. The lines C_m describe the grooves of a generic 2D grating. It is assumed that each point S, with polar coordinates (ρ, Ψ) scatters a portion of the SWs out of the plane, while the other portion keeps propagating along the surface. The radiation pattern of this system is obtained by summing over all scattered fields.

It is assumed that the field $dE_S(r)$ scattered by an infinitesimal portion of C_m around S, subtending an angle $d\Psi$ can be modeled by that of an electric dipole located at S, and having an amplitude proportional to the amplitude of the SW at that point, modulated by a scattering efficiency. The SW complex amplitude at S can be expressed as $a_S = f_1(\rho)f_2(\Psi)\exp(ik_{sw}\rho)$, where $f_1(\rho)$ expresses the decay of the SWs as they propagate away from the source (due to diffraction, scattering, and absorption losses), and $f_2(\Psi)$ is the angular distribution of the SWs launched at the point source. k_{sw} is the SW wavevector.

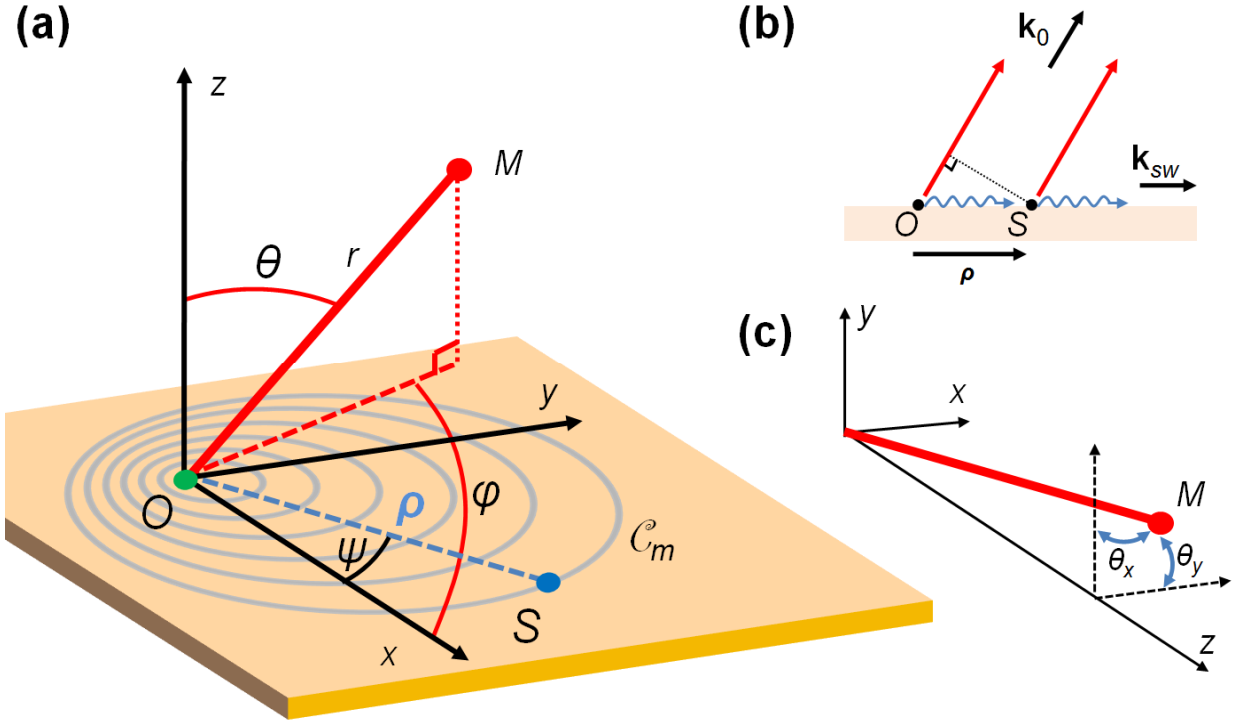


Fig. 11 (a) Schematic of a plasmonic lens. (b) Interference between the field radiated by the source O and the field scattered by S. (c) Definition of the angle system (θ_x, θ_y) .

For a point source polarized at an angle $\Psi = \Psi_S$, $f_2(\Psi)$ can be expressed as $f_2(\Psi) = \cos(\Psi - \Psi_S)$. As the lines of scatterers represent grooves, the orientation of the dipole is taken in the x-y plane, normal to the groove. Qualitatively, this choice stems from the picture of an incident SW driving charge oscillations on one edge of the groove, which in turn triggers oscillations of image charges on the opposite edge, at the shortest distance and thus in the direction normal to the groove. Polarization sensitive experimental results will corroborate this assumption..

If $\hat{\delta}$ is a unit vector which defines the orientation of the dipole, δ being the angle formed with the x-axis, one can write:

$$d\mathbf{E}_S(\mathbf{r}) \propto a_S f_3(\delta - \psi) \frac{e^{i(k_0 \hat{\mathbf{n}} \cdot (\mathbf{r} - \boldsymbol{\rho}) + c_1)}}{r} [(\hat{\mathbf{n}} \times \hat{\boldsymbol{\delta}}) \times \hat{\mathbf{n}}] d\psi$$

where $\hat{\mathbf{n}}$ is the unit vector in the direction OM. The source is assumed monochromatic, with a free-space wavelength $\lambda = 2\pi/k_0$. The reflections of SWs at the grooves are neglected, which is a valid approximation except in the case of constructive interference of the small reflections from each groove, which sets in when the grating period is about $m\lambda_{SW}/2$ where $m=1,2,3,\dots$. The groove scattering efficiency at S is denoted by $f_3(\delta - \Psi)$. It depends on the direction of the incident SW relative to the groove, and on the groove depth and width. The phase shift introduced by the scattering event is c_1 .

The expression of the total field is obtained by summing over the continuous distribution of scatterers S on the line C_m , and over N lines. The radiated power density in the far-field is proportional to the angle-dependant component of $|\mathbf{E}(r)|^2$:

$$D(\theta, \varphi) \propto \left| \sum_{m=1}^N \int_0^{2\pi} e^{i\Delta\phi} f_1 f_2 f_3 \hat{e}(\theta, \varphi, \delta) d\psi \right|^2$$

where :

$$\hat{e}(\theta, \varphi, \delta) = \cos(\theta) \cos(\delta - \varphi) \hat{\theta} + \sin(\delta - \varphi) \hat{\phi}$$

$\Delta\phi$ is the phase difference between the field \mathbf{E}_S scattered by S and the field \mathbf{E}_0 directly emitted from the source O, both evaluated at point M with spherical coordinates (r, θ, φ) in the far-field. It is given by:

$$\Delta\phi = k_{sw} \hat{\mathbf{m}} \cdot \boldsymbol{\rho} - k_0 \hat{\mathbf{n}} \cdot \boldsymbol{\rho} + c_1$$

where $\hat{\mathbf{m}}$ is the unit vector in the direction OS.

The model developed here enables one to calculate the far-field radiation pattern of any 2D grating, once the equation of the curves C_m is known. Of particular interest is the problem of a grating that would scatter SWs originating from a point source into a collimated free-space beam of arbitrary direction (θ, φ) .

The equation of the curves C_m for such a grating is obtained by requiring constructive interference in that specific direction. This condition is $\Delta\phi = m2\pi$, m being an integer. Introducing the SW effective index n_{sw} , one obtains the equation that yields the position of the scatterers:

$$\rho = \rho_m(\psi) = \lambda_0 \frac{m - c_1/2\pi}{n_{sw} - \sin(\theta) \cos(\psi - \varphi)}$$

This equation states that the scatterers must be located on the curves C_m defined by the polar equations $\rho = \rho_m(\Psi)$ for all emitted fields to constructively interfere in the direction (θ, φ) . The curves C_m are ellipses with the origin O at one of their foci.

The experimental set-up scans the far-field in the angle system (θ_x, θ_y) , which are the angles with respect to the z-axis projected on the planes x-z and y-z (Fig 11(c)).

One is now able to calculate the far-field patterns of the elliptical gratings. Note that the input parameters of the model, specific to a given groove geometry and working wavelength, can be readily determined through simple considerations and 2D simulations as shown thereafter for a particular structure. The simulations used here require orders of magnitude less resources (in time and memory) than the 3D simulations one would need to simulate the final device. Importantly, once these parameters have been evaluated, it is possible to study the response of all sorts of gratings by simply changing the equation of the curves C_m , predicting not only the amplitude pattern but also the phase pattern of the radiated light.

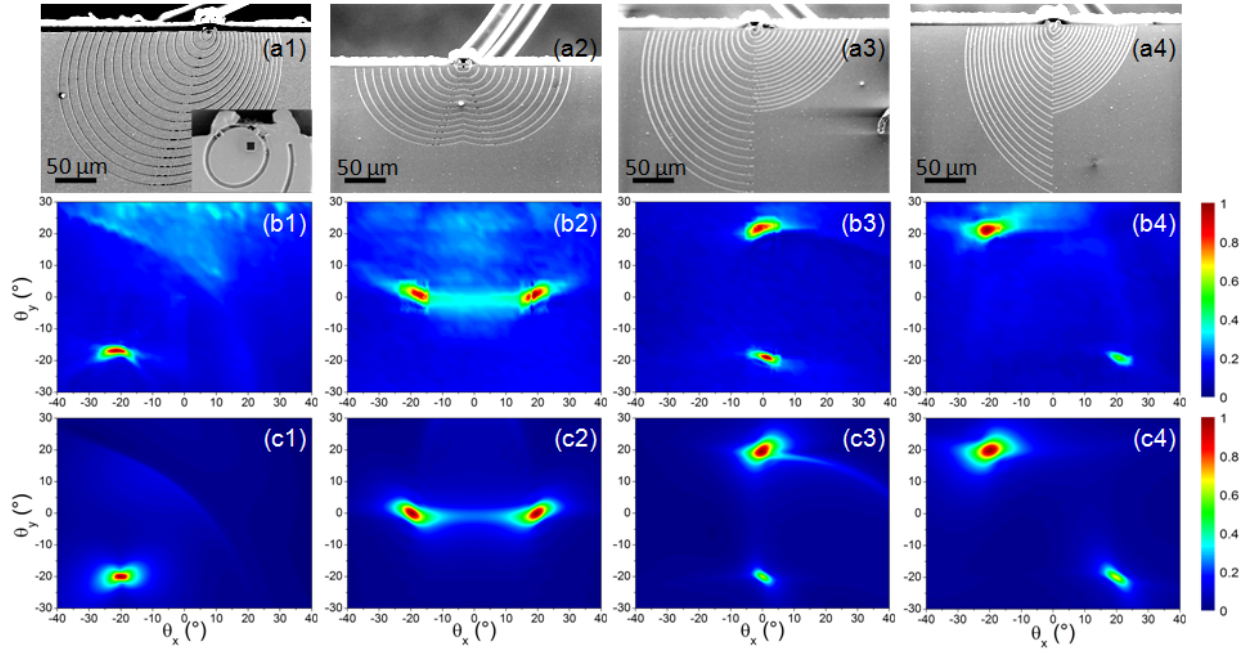


Fig 12. Four different plasmonic lenses producing one (a1) or two (a2, a3, a4) beams, fabricated on the facet of quantum cascade lasers. For each structure, we show an SEM image (a), and the measured (b) and calculated (using the model we develop herein) (c) far-field intensity (normalized to 1). The inset in (a1) is a close-up image of a typical aperture. The measured far-fields are obtained by scanning a liquid-nitrogen-cooled mercury-cadmium-telluride detector, positioned 10-20 cm away from the device, over θ_x and θ_y , with a resolution of 0.5° .

b. Simulations and fabrication

In order to demonstrate that such elliptical gratings can act as plasmonic lenses, the structures are fabricated directly on the gold-coated facet of mid-infrared quantum cascade lasers emitting at $\lambda=8.06\mu\text{m}$. Note that the concept is general and such lenses can be implemented on any structure supporting surface waves or quasi-two-dimensional optical modes (e.g. slab waveguides). It is also scalable to other spectral ranges.

2Ds simulations were performed of a 1D grating, using a commercial FEM simulation package (COMSOL Multiphysics), in order to design the groove parameters and extract the relevant parameters. Groove depth and width of $1\mu\text{m}$ have been found to maximize the peak intensity of the collimated beam for a grating comprising 10 to 20 grooves. This optimization relies on a trade-off between the grooves scattering efficiency and the amount of energy reaching the last grooves.

Fig. 12(a1) shows a scanning electron microscope (SEM) image of a representative fabricated grating, designed to emit light in the direction ($\theta_x=-20^\circ, \theta_y=-20^\circ$). In this device, the point-like source of SWs is an aperture opened in the metal film (inset in Fig. 12(a1)). The light in the laser waveguide impinges on the back side of the aperture,

launching surface waves on the grating-air interface, along with some directly transmitted light.

The point-like character of the aperture stems from its subwavelength dimensions ($2\mu\text{m} \times 2\mu\text{m}$ for $\lambda = 8.06\mu\text{m}$).

The fabrication process involves focused ion beam (FIB) milling to sculpt $1\mu\text{m}$ -wide and $1\mu\text{m}$ -deep grooves into the semiconductor facet (indium phosphide), then deposition of 250 nm of alumina, acting as an insulation layer, followed by 250 nm of gold. The small aperture in the metal film is eventually opened using FIB. As can be seen in Fig. 12(a1), only a portion of the grating is fabricated because of the geometry of our laser facet.

c. Measurements

Fig.12 (b1) presents the measured far-field of the device shown in Fig. 12(a1), which is composed of 13 grooves. The angular divergence, defined as the full width at half maximum (FWHM), is about 8 degrees along θ_x and 3 degrees along θ_y . This divergence angle is comparable to those obtained with simple circular collimator designs and represents a dramatic improvement compared to the divergence angles of about 40 degrees along θ_x and 70 degrees along θ_y for the original unpatterned laser. The small discrepancy between our data and the designed angular direction is due to misalignment of the far-field measurement set-up. Note that a residual signal is visible in the upper part of the measured far-field, mainly due to light emitted from the back facet of the laser reaching the detector after undesired reflection on the laser mount. To suppress this signal, high reflection coatings have been applied to the back facets of the devices subsequently fabricated (a2, a3 and a4). Moreover, a background, which is measured to be $\sim 10\%$ of the maximum intensity, is present. As only a small portion of the light throughput is coupled into the SWs, the destructive interference between the fields scattered by the grooves and the strong direct emission from the aperture is not complete. This results in the background observed. This coupling efficiency could be greatly increased by patterning the metal around the aperture with sub-wavelength grooves to reduce the wavevector mismatch between the laser waveguide mode and the SWs, as was demonstrated in the terahertz range by the PI group (Yu *et al. Nature Materials* **9**, 730 (2010)). These data demonstrate that a suitable elliptical 2D plasmonic grating transforms a point source of SWs located at the focal point into a collimated free-space beam in a tailorable direction, i.e. it acts as planar plasmonic lens.

\One can design a plasmonic lens with a single focus capable of forming several beams in arbitrary preselected directions. This is achieved by placing portions of different gratings side by side on the facet. The PI group fabricated three different structures (Fig.12(a2,a3,a4), each designed to collimate light in two specific directions, respectively ($\theta_x = \pm 20$ degrees, $\theta_y = 0$) with $N=13$ grooves, ($\theta_x = 0$, $\theta_y = \pm 20$ degrees) with $N=19$ and ($\theta_x = \pm 20$ degrees, $\theta_y = \mp 20$ degrees) with $N=20$. The results are presented in Fig. 12 (columns 2, 3 and 4), where both the measured (b) and calculated (c) far-field intensity are plotted. The two collimated beams are clearly distinguishable for each plasmonic lens, proving the robustness of the concept.

Fig. 12(c) shows the radiation pattern emitted by the four structures in Fig. 12(a), calculated using our model and considering a source polarized along y ($\Psi_S = \pi/2$). In this calculation of $\mathbf{E}(\mathbf{r})$ only the fields scattered by the grating were included. The other contributions due for example to the light directly radiated at the aperture will contribute to the background but will not alter significantly the shape of the collimated beam.

For each plasmonic lens, the agreement between calculated and measured data (Fig. 12(b)) is good. The shape of the collimated beams is well reproduced, and the measured divergence angle is generally close to the calculated one (relative error of 15% in average). The discrepancies are mainly attributed to fabrication defects, in particular the presence on the grating surface of dust particles that open additional scattering channels and reduce the propagation length of the SWs.

The finite size of the spot is determined by the SW decay and the size of the grating. Previous demonstrations of multi-beam emission from semiconductor lasers relied on simple 1D gratings which resulted in asymmetric beam shapes and gave limited control over the direction of emission. The application of our dipolar model has made it possible to overcome these limitations by facilitating the design of more complex grating structures.

Note that the model presented here should be particularly valuable for designing new plasmonic components featuring complex phase responses, which could generate, for example, Bessel beams or optical vortices.

7. Publications

1. Nanfang Yu, Qijie Wang, Federico Capasso, “Beam engineering of quantum cascade lasers” *Laser & Photonics Reviews* **6**, 26 (2012) *Invited Review and Cover story of the Jan. 2012 Issue*
2. J-P Tetienne, R Blanchard, N Yu, P Genevet, M A Kats, J A Fan, T Edamura, S Furuta, M Yamanishi, F Capasso, “Dipolar modeling and experimental demonstration of multi-beam plasmonic collimators” *New Journal of Physics* **13**, 53057 (2011)
3. Qi Jie Wang, Changling Yan, Nanfang Yu, Julia Unterhinninghofen, Jan Wiersig, Christian Pflugl, Laurent Diehl, Tadataka Edamura, Masamichi Yamanishi, Hirofumi Kan, Federico Capasso, “Whispering-gallery mode resonators for highly unidirectional laser action” *Proc. Natl. Acad. Sci. USA* **107**, 22407 (2010). *A commentary article appeared in the same issue: Marlan O. Scully: “Collimated unidirectional laser beams from notched elliptical resonators” Proc. Natl. Acad. Sci. USA* **107**, 22367 (2010)
4. Martina Hentschel, Qi Jie Wang, Changling Yan, Federico Capasso, Tadataka Edamura, Hirofumi Kan, “Emission properties of electrically pumped triangular shaped microlasers”, *Optics Express* **18**, 16437 (2010)

5. Qi Jie Wang, Changling Yan, Laurent Diehl, Martina Hentschel, Jan Wiersig, Nanfang Yu, Christian Pflugl, Mikhail A Belkin, Tadataka Edamura, Masamichi Yamanishi, Hirofumi Kan, Federico Capasso, "Deformed microcavity quantum cascade lasers with directional emission" *New Journal of Physics* **11**, 125018 (2009)
6. Changling Yan, Qi Jie Wang, Laurent Diehl, Martina Hentschel, Jan Wiersig, Nanfang Yu, Christian Pflugl, Federico Capasso, Mikhail A. Belkin, Tadataka Edamura, Masamichi Yamanishi, Hirofumi Kan, "Directional emission and universal far-field behavior from semiconductor lasers with limaçon-shaped microcavity" *Applied Physics Letters* **94**, 251101 (2009)

8. **Inventions or patent disclosures:**

HU3994 "Highly Unidirectional Microcavity Lasers" international (PCT) patent application filed on 11/29/2011. Inventors: Federico Capasso, Nanfang Yu, Qi Jie Wang, Julia Unterhinninghofen, Jan Wiersig.
